

# LII–lidar: range-resolved backward picosecond laser-induced incandescence

Billy Kaldvee · Christian Brackmann ·  
Marcus Aldén · Joakim Bood

Received: 11 September 2012 / Accepted: 6 July 2013 / Published online: 20 July 2013  
© Springer-Verlag Berlin Heidelberg 2013

**Abstract** A novel concept for remote in situ detection of soot emissions by a combination of laser-induced incandescence (LII) and light detection and ranging (lidar) is presented. A lidar setup based on a picosecond Nd:YAG laser and time-resolved signal detection in the backward direction was used for LII measurements in sooty premixed ethylene–air flames. Measurements of LII–lidar signal versus laser fluence and flame equivalence ratio showed good qualitative agreement with data reported in literature. The LII–lidar signal showed a decay consisting of two components, with lifetimes of typically 20 and 70 ns, attributed to soot sublimation and conductive cooling, respectively. Theoretical considerations and analysis of the LII–lidar signal showed that the derivative was proportional to the maximum value, which is an established measure of soot volume fraction. Utilizing this, differentiation of LII–lidar data gave profiles representing soot volume fraction with a range resolution of  $\sim 16$  cm along the laser beam propagation axis. The accuracy of the evaluated LII-profiles was confirmed by comparison with LII-data measured simultaneously employing conventional right-angle detection. Thus, LII–lidar provides range-resolved single-ended detection, resourceful when optical access is restricted, extending the LII technique and opening up new possibilities for laser-based diagnostics of soot and other carbonaceous particles.

## 1 Introduction

Soot is a well-known combustion pollutant and formation of soot as well as other nanometer-size particles in combustion has been studied extensively [1, 2]. The negative environmental impact as well as toxicity effects to organisms makes reduction of soot and other nanoparticle emissions a highly relevant issue [3, 4]. A number of methods for detection and characterization of soot-particle emissions exist; many of them are probe techniques based on sampling and able to provide quantitative measures [5, 6]. In contrast to sampling methods, a range of optical techniques instead provide soot measurements in situ [6].

Laser-induced incandescence (LII) [7, 8] is a technique used for soot detection and characterization, measuring the black-body radiation emitted from particles rapidly heated by laser radiation. The LII technique allows for measuring soot volume fraction,  $f_v$ , and particle sizes, both spatially and temporally resolved, and has been applied in flames, combustion engines, and exhaust gases [7]. The basic physical mechanisms usually accounted for, when modeling the LII process, are absorption of laser radiation, black-body emission (Planck radiation), heat conduction, and soot sublimation. Intensive modeling work has been conducted during the last decades, based on the pioneering LII model by Melton [9], who concluded that the LII-signal,  $S_p$ , from a soot particle was proportional to  $D^x$ , where  $D$  designates the primary particle diameter and  $x = 3 + 0.154/\lambda_{\text{det}}$ , with  $\lambda_{\text{det}}$  being the detection wavelength expressed in  $\mu\text{m}$ .

Assuming that the total LII-signal,  $S_t$ , can be retrieved from the product of the signal from an individual particle and the particle number density in the measurement volume,  $S_t$  becomes nearly proportional to  $f_v$ , which has a cubic dependence on  $D$ . The deviation depends on the

B. Kaldvee (✉) · C. Brackmann · M. Aldén · J. Bood  
Division of Combustion Physics, Lund University, Box 118,  
221 00 Lund, Sweden  
e-mail: billy.kaldvee@forbrf.lth.se

effects of sublimation and conduction. Bladh et al. [10] have in detail investigated the dependence of the LII-signal on soot volume fraction for variations in particle size, concluding that the effect of sublimation can be avoided by using low laser fluence and that the effect of conduction can be minimized by collecting the prompt LII-signal with shortest possible detector gate. Moreover, in the same work, it was concluded that longer detection wavelengths and a uniform spatial profile of the laser beam, i.e., a tophat profile, are preferred for achieving a nearly linear relationship between  $S_t$  and  $f_v$ .

Traditionally, LII measurements have been made with right-angle detection perpendicular relative to the laser beam propagation path. However, sometimes the lack of optical access prohibits this and for such cases a backward detection scheme has been investigated [11] and also applied in aero-engine exhausts [12–14]. The pure backward detection scheme is, however, a line-of-sight measurement, yielding no range resolution along the laser beam path. For imaging backward detection, the detected LII-signal can be analyzed over a small region of the laser beam profile to extract an LII-signal generated with homogenous laser fluence also for Gaussian beams [11], a possibility not available for data acquired with right-angle detection. Semi-backward configuration, with a camera placed at an angle of  $9^\circ$  relative to the laser beam path has been proposed and demonstrated by Jenkins et al. [15]. The angled imaging allows for a range resolution of 5 cm over a 1 m range along the laser beam path. Nevertheless, a technique for genuine single-ended detection of soot with maintained range resolution would clearly be beneficial for soot diagnostics under conditions with limited optical access.

Light detection and ranging (lidar) is a measurement technique for single-ended range-resolved detection of laser-induced light-emitting events. Lidar utilizes the fact that the time,  $t$ , it takes for laser light to propagate back and forth over a distance  $R$  is given by  $t = 2R/c$ . Consequently, using a pulsed laser, the range resolution,  $\delta R$ , of a lidar experiment is ultimately governed by the laser pulse duration,  $\delta t$ , as  $\delta R = c \times \delta t/2$ . Traditionally, lidar has been used for long-range (km) studies of atmospheric properties, such as temperatures, species concentrations, and wind flows [16, 17], but has also recently been demonstrated using picosecond laser pulses for temperature and species measurements in combustion diagnostics [18, 19]. The ultimate range resolution of lidar measurements employing laser pulse durations shorter than 100 ps is better than 1.5 cm and in many cases limited by the temporal response of the detector. Photo-multiplier tubes (PMT) have temporal resolutions on the order of hundreds of picoseconds, while streak cameras [20, 21], although having less light collection efficiency, may have temporal

resolutions on the order of a few picoseconds. Thus, detection down to millimeter-scale range resolution is readily attainable and adequate for measurements in combustion devices of size  $\sim 1$ –10 m.

In this work, ps-lidar for range-resolved, single-ended LII diagnostics is demonstrated by time-resolved backward detection of LII-signals from premixed ethylene–air flames burning on porous plug burners. The temporal characteristics of LII-signals induced with picosecond pulses has been investigated by Michelsen with modeling as well as experiments, using 532 nm laser radiation and right-angle signal collection geometry. In particular, the prompt 500 ps of the picosecond-induced LII-signal were characterized in detail with high temporal resolution [22, 23]. However, the LII–lidar experiments presented in this paper in several aspects differ from the picosecond investigations of Michelsen. Firstly, particle heating is induced with 1,064 nm radiation, which effectively avoids interference from PAH fluorescence [13, 23]. Secondly, signals are collected with backward detection, which in some aspects differ from right-angle detection [11], for example profile hole-burning at high laser fluence is more clearly revealed and different signal absorption may also occur. Finally, for LII–lidar, the signal emitted at times much later than the 500 ps interval characterized by Michelsen is used.

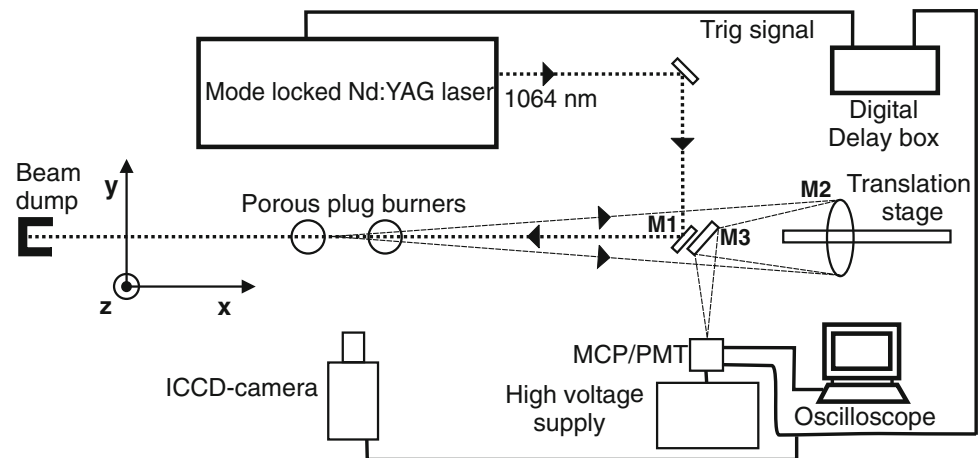
Thus, this work includes investigations of the dependence on laser fluence of the signal and its temporal characteristics on a longer time scale, both necessary for characterization of the LII–lidar method. Furthermore, the dependence on flame equivalence ratio was studied to compare the soot detection ability with that of conventional LII as presented in previously published LII-data. A method to evaluate the LII–lidar signal, for range-resolved mapping of  $f_v$ , was investigated for measurements in two flames. The obtained spatial soot volume fraction profiles are compared with results from simultaneous LII measurements using right-angle detection. The presented LII–lidar concept fulfills many of the demands for proper soot volume fraction measurement using LII: particles are heated with 1,064 nm radiation, signal detection includes long wavelengths, and the evaluation scheme results in data equivalent to the prompt LII-signal. In addition, the abilities of LII for soot probing are extended with range-resolved single-ended detection, valuable for conditions with limited optical access, and improved remote sensing.

## 2 Experimental

### 2.1 Lidar setup

The experimental setup is schematically outlined in Fig. 1. The fundamental 1,064 nm radiation of a mode-locked

**Fig. 1** Schematic illustration of the experimental setup for LII-lidar. Pulses from a picosecond Nd:YAG laser are directed into the measurement region by mirror M1. LII-radiation from heated soot above the porous plug burners is collected by a concave mirror, M2, and directed by a planar mirror, M3, to a photomultiplier tube (MCP-PMT). For comparison, an ICCD camera is used for simultaneous right-angle LII measurements



Nd:YAG laser (Ekspla, PL 2143C) with a pulse duration of 80 ps and a repetition rate of 10 Hz was used as light source. The laser beam  $1/e^2$  diameter has been measured to 11.6 mm. The laser beam was directed toward the measurement objects using a planar protected aluminum mirror, M1. The measurement objects were two water-cooled porous-plug burners (McKenna, Holthuis & Associates) with stabilization plates mounted 21 mm above them. The burners were fed with ethylene and air via mass-flow controllers (Bronkhorst). One of the burners was placed on a carriage movable along the  $x$ -axis.

The signal was collected in the backward direction using a Newtonian-style telescope having a concave 10-cm-diameter aluminum-coated primary mirror, M2, with focal length 45 cm. The primary mirror was placed on a computer-controlled 30-cm translation stage, allowing adjustable position of the focal plane. The collected light was directed toward the detector using a planar mirror, M3. The signal was detected with a micro-channel-plate photomultiplier tube (MCP-PMT) (Hamamatsu R5916U-50), which allows time-gated detection for background suppression. The detector response is characterized by quantum efficiencies 0.15, 0.055, and  $2.5 \times 10^{-4}$  at 400, 600, and 780 nm, respectively, and by rise- and falltimes of 170 and 730 ps, respectively. The PMT signal was recorded on a 3 GHz bandwidth digital oscilloscope (Lecroy Wavemaster 8300). For comparison with the backscattered LII-signals, an ICCD camera (PI-MAX 3, Princeton Instruments) was positioned perpendicular to the laser beam for right-angle LII measurements. LII images were collected using  $f = 50$  mm (Nikkor  $f/1.2$ ) and  $f = 24$  mm (Nikkor  $f/2.8$ ) objectives.

Figure 2a shows a photo of the measurement objects positioned in the laser beam path that is indicated with a green line passing through the two flames. The LII-signal detected with the ICCD camera at right angle is shown in

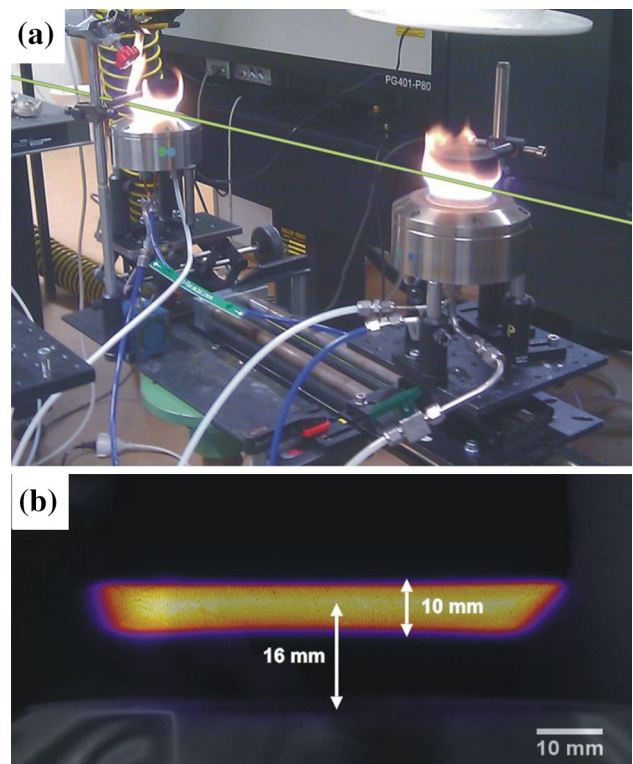


**Fig. 2** **a** Photo showing the porous-plug burners positioned in the laser beam path, indicated by the green line. The right burner was mounted on a rail for translation along the beam path. **b** LII-signal (blue-yellow) detected at right angle in one of the burners (grayscale). The center of the measurement volume and signal is located  $\sim 16$  mm above the burner surface

blue-red-yellow color map in the overlay image of Fig. 2b, which also shows the burner in grayscale. The measurement volume, 10 mm wide, is centered approximately 16 mm above the burner surface. The signal recorded by the MCP-PMT is integrated over the entire height of the measurement volume, setting the vertical resolution of the

lidar measurements using this experimental setup to be determined by the laser beam diameter. Nevertheless, the vertical resolution can be improved by reducing the laser beam diameter and/or by positioning a horizontal slit in front of the MCP-PMT, the latter, however, decreasing the signal collection.

## 2.2 Measurements

For correct interpretation of an LII-signal, it is necessary to discriminate it from the nascent flame emission as well as interferences from scattered laser radiation [7]. For this purpose, LII-signals are often detected using a short-pass filter with transmission in the blue wavelength regime [7]. In the present LII-lidar setup, however, the detector had very low sensitivity at 1,064 nm and no interference from scattered radiation was obtained. Moreover, with time-resolved detection, the continuous flame emission only contributes with a constant background level that can be easily compensated for in data evaluation. Data collected both with and without a 425-nm short-pass detection filter show similar trends, however, with higher signal-to-noise ratio for the latter. Thus, the data presented in this paper were acquired without filter.

For measurements of the dependence on laser fluence of the LII-lidar signal, one of the burners was positioned at 2 m distance from the telescope mirror, M2. The flame equivalence ratio was 2.1 with a total gas flow of 10 l/min. The laser fluence, calculated using the  $1/e^2$  beam diameter, was varied in 40 steps ranging from 0.045 to 0.215 J/cm<sup>2</sup>. For each laser fluence, the LII-lidar signal was accumulated over 300 laser pulses.

An investigation of the equivalence ratio dependence of the LII-lidar signal was carried out in two measurement series employing the laser fluences 0.1 and 0.2 J/cm<sup>2</sup>, respectively. The flame equivalence ratio was varied from 1.8 to 3.0 having the total reactant gas flow kept at 10 l/min. The data at each equivalence ratio were accumulated over 600 laser pulses. In order to measure the range-resolved soot volume fraction distribution, the final measurements were made using two burners simultaneously. The flame equivalence ratios were 2.1 with a gas flow of 9 l/min through each burner. Two measurement series were conducted with the laser fluence set to 0.07 and 0.19 J/cm<sup>2</sup>, respectively. The center-to-center distance between the burners along the  $x$ -axis was varied in six steps: 0.21, 0.24, 0.27, 0.30, 0.40, and 0.50 m, respectively. Each recording was accumulated over 600 laser pulses. To facilitate the interpretation of the lidar results, the ICCD camera was used in a right-angle setup for two-dimensional detection of the LII-signal using a 100 ns gate.

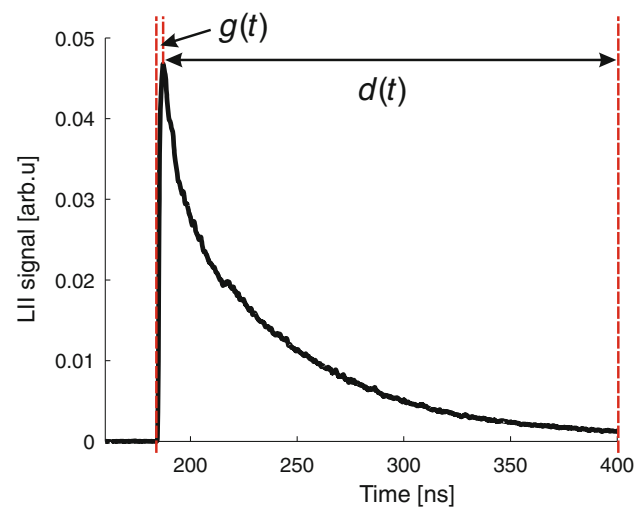


**Fig. 3** A typical ps-LII-signal measured with the LII-lidar setup. The part of the curve where the signal increase is defined as  $g(t)$  and the decay part of the curve is defined as  $d(t)$

## 3 LII-lidar

A LII-signal detected with ps-lidar,  $S(t)$ , may be expressed as the sum of the individual time-resolved LII-signals,  $p_x(t)$  from each spatial position,  $x$ . Lidar signals from positions separated with distance  $\Delta x$  will be shifted  $\Delta t = 2\Delta x/c$  in time [18]. A typical ps-LII-signal, shown in Fig. 3, measured with the present LII-lidar setup, consists of a signal increase function,  $g(t)$ , having a risetime on the order of 1 ns, and a decay function,  $d(t)$ , having a lifetime of hundreds of nanoseconds. Michelsen showed, in measurements with high temporal resolution,  $\sim 8$  ps, and laser pulse duration of 65 ps FWHM, that the risetime of the LII-signal,  $\tau_r$ , is on the same order of magnitude as the laser pulse duration [23]. For the ps-lidar measurements demonstrated in this paper, the detected LII-signal's increase function,  $g(t)$ , is however governed by the rise- and fall-time, 170 and 730 ps, respectively, of the MCP-PMT.

The emitted LII-lidar signal  $S(t)$  can be written as the sum of the signal increase function of the emitted LII-signal,  $g_x^{\text{real}}(t)$ , and decay curve contribution,  $d_x(t)$ , from every spatial position in the measurement area. The LII-lidar signal contribution from positions  $x > ct/2$ , ahead of the laser pulse at time  $t/2$ , is 0; therefore,  $ct/2$  is set as the upper summation limit.

$$\begin{aligned}
 S(t) &= \sum_{x=0}^{ct/2} p_x \left( t - \frac{2x}{c} \right) = \sum_{x=0}^{ct/2} \left[ g_x^{\text{real}} \left( t - \frac{2x}{c} \right) + d_x \left( t - \frac{2x}{c} \right) \right] \\
 &= \underbrace{\sum_{x=0}^{ct/2} g_x^{\text{real}} \left( t - \frac{2x}{c} \right)}_I + \underbrace{\sum_{x=0}^{ct/2} d_x \left( t - \frac{2x}{c} \right)}_{II}
 \end{aligned} \tag{1}$$

In the results section, it will be shown that the decays of experimental LII-signals, acquired using the lidar setup, with good agreement can be fitted to double exponential functions. Thus, in the following theoretical analysis, the decay functions are represented by double exponential functions with decay constants  $\alpha_1$  and  $\alpha_2$  and term II of Eq. (1) can be expressed as:

$$\begin{aligned} & \sum_{x=0}^{ct/2} \left[ C_{1x} e^{-\alpha_1(t-2x/c)} + C_{2x} e^{-\alpha_2(t-2x/c)} \right] \\ &= \sum_{x=0}^{ct/2} \left[ C_{1x} e^{-\alpha_1 t} e^{2\alpha_1 x/c} + C_{2x} e^{-\alpha_2 t} e^{2\alpha_2 x/c} \right] \\ &= e^{-\alpha_1 t} \sum_{x=0}^{ct/2} C_{1x} e^{2\alpha_1 x/c} + e^{-\alpha_2 t} \sum_{x=0}^{ct/2} C_{2x} e^{2\alpha_2 x/c} = K_{1t} e^{-\alpha_1 t} \\ & \quad + K_{2t} e^{-\alpha_2 t} \end{aligned} \tag{2}$$

The interpretation of Eq. (2) is that the total contribution of all LII-signal sources being in the decay curve phase will decay with decay constants  $\alpha_1$  and  $\alpha_2$ . The constants  $K_t$  represent a virtual accumulated signal level at time  $t = 0$  if all LII sources between  $x = 0$  and  $x = ct/2$  would have been positioned at  $x = 0$ . Relative to a specific time,  $\tau$ , for  $t > \tau$ , the last term of Eq. (2) can be rewritten as:

$$K_{1t} e^{-\alpha_1 t} + K_{2t} e^{-\alpha_2 t} = K_{1\tau} e^{-\alpha_1(t-\tau)} + K_{2\tau} e^{-\alpha_2(t-\tau)} \tag{3}$$

where  $K_{1\tau}$  and  $K_{2\tau}$  represent the total signal contribution from all  $d_x(t)$  at time  $\tau$ . Since the risetime of the emitted LII-signal,  $\tau_r$ , is very short,  $\sim 80$  ps, in comparison with the lifetime of the decay curve,  $> 60$  ns, term II is generally much greater than term I in Eq. (1). Hence, the sum of the  $K_{1\tau}$  and  $K_{2\tau}$  terms may be estimated as the whole signal,  $S(t)$ , at time  $\tau$ . Using the results from Eqs. (2) and (3), Eq. (1) can be expressed as:

$$\begin{aligned} S(t) &= \sum_{x=0}^{ct/2} g_x^{\text{real}} \left( t - \frac{2x}{c} \right) + K_{1\tau} e^{-\alpha_1(t-\tau)} + K_{2\tau} e^{-\alpha_2(t-\tau)} \\ &= G(t) + K_{1\tau} e^{-\alpha_1(t-\tau)} + K_{2\tau} e^{-\alpha_2(t-\tau)} \end{aligned} \tag{4}$$

The time derivative,  $S'(\tau)$ , of Eq. (4) can be rewritten into an expression for the time derivative of the signal increase function,  $G'(\tau)$  according to Eq. (5):

$$\begin{aligned} S'(\tau) &= G'(\tau) - \alpha_1 K_{1\tau} - \alpha_2 K_{2\tau} \Rightarrow G'(\tau) \\ &= S'(\tau) + \alpha_1 K_{1\tau} + \alpha_2 K_{2\tau} \end{aligned} \tag{5}$$

It can readily be seen that if the lifetimes,  $1/\alpha_1$  and  $1/\alpha_2$ , are long enough compared with the lidar measurement time window,  $\Delta t = 2\Delta x/c$ , the time derivative of the signal will be dominated by the contribution from LII-signals in their signal increase phase,  $G(t)$ .

In the results section, it will be shown that  $G'(t)$ , as could be expected in most cases, is proportional to  $S_{\text{max}}(t)$ , which in turn is a very good representation of the prompt LII-signal that would be collected using a short detection gate. Accordingly,  $G'(t)$  is proportional to the soot volume fraction [10]. Hence, knowing the decay rates,  $\alpha_1$  and  $\alpha_2$ , and assuming them constant in the measurement volume, as well as neglecting laser extinction and signal absorption, it is possible to calculate a range-resolved soot volume fraction distribution, which will be shown in the result section. Utilizing Eq. (5), it is also possible, for validation purposes, to recreate a signal corresponding to  $\alpha = 0$ , denoted  $S_{\alpha=0}(t)$ , which should be constant when the laser pulse has passed the soot situated in a measurement volume of length  $x_{\text{meas}}$ , at times  $t > 2x_{\text{meas}}/c$ .

## 4 Results and discussion

### 4.1 Fluence dependence

Three typical lidar curves acquired in one burner at different laser fluences are shown in Fig. 4, where the time interval of 20 ns corresponds to a spatial range of 3 m. The curves show a rapid increase, reaching their maximum value within a few nanoseconds (cf. Fig. 3), determined by the temporal characteristics of the detector, as discussed previously. In time-resolved LII measurements, Michelsen has observed an increase in signal growth rate and decrease in risetime with laser fluence [23], which means faster heating and soot sublimation with signal losses induced earlier during the laser pulse. The reported differences in risetime for picosecond LII are on the order of tens of picoseconds [23] and thus smaller than the temporal resolution of the data presented here. Nevertheless, the LII-

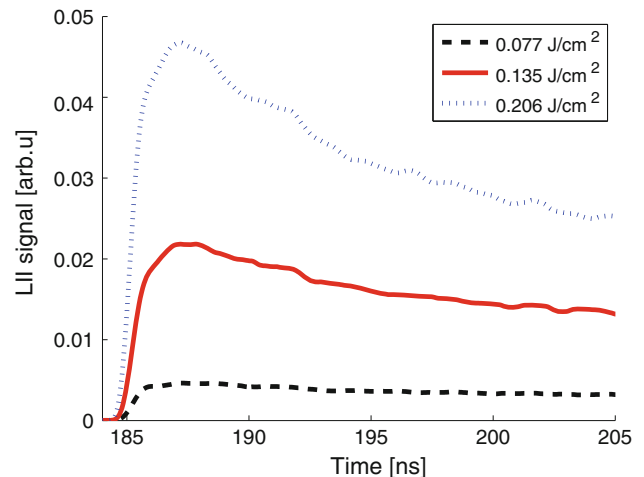
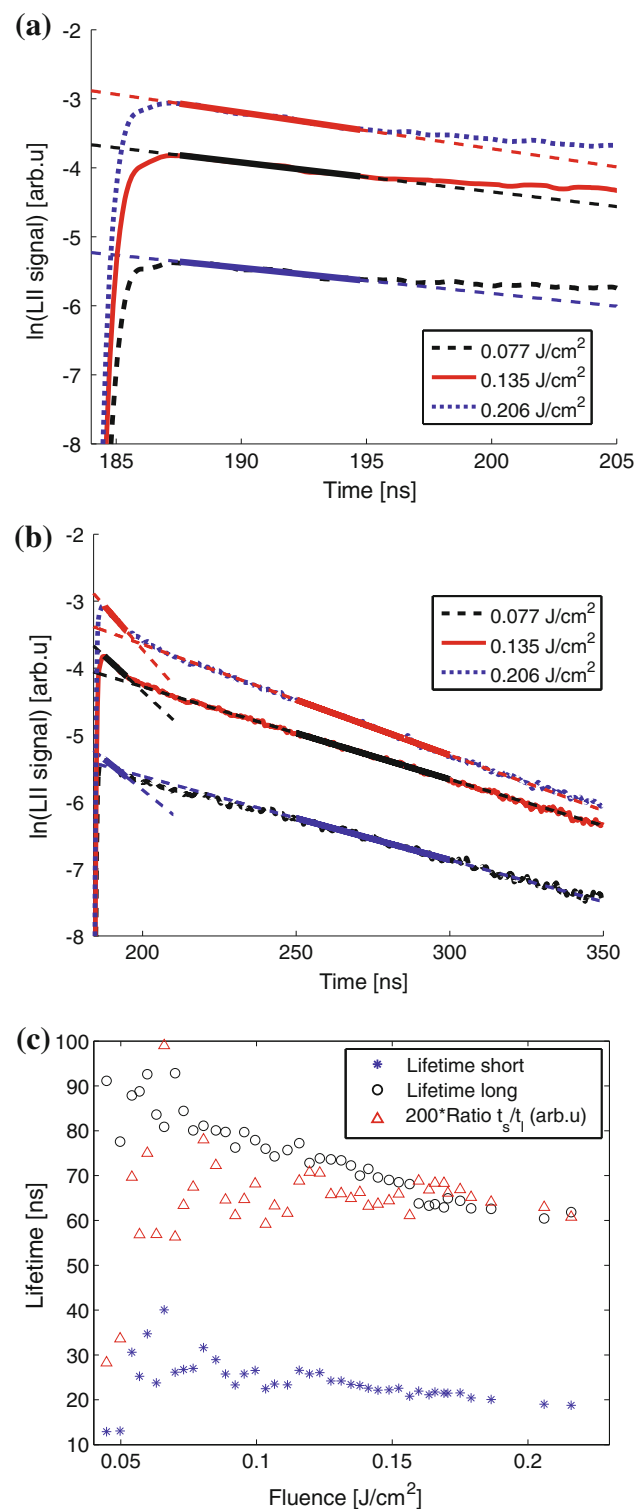


Fig. 4 LII-lidar curves obtained from measurements on an ethylene-air flame with  $\Phi = 2.1$  using three different laser fluences

lidar curves presented in Fig. 4 also show a steeper signal rising edge with increasing laser fluence. One of the main challenges in LII modeling is to predict the sublimation effects [22]. From that point of view, low fluences are preferred for interpretation of time-resolved LII while utilizing extended LII models taking effects as annealing, oxidation, and photodesorption into account [22].

The natural logarithms of the LII-signals are presented in Fig. 5a, b and the data can be piecewise fitted to straight lines with very good agreement, confirming that the signals closely resemble double exponential decays. In Fig. 5a, using the same time axis as Fig. 4, it is seen that the first 10 ns, between 185 and 195 ns, are dominated by a fast decay having a short life time,  $\tau_{\text{short}}$ , decreasing with increasing fluence. The physical origin of this fast decay process, which is insufficiently described in the present LII models, is still an open issue for research [24]. In LII using laser wavelength 532 nm for particle heating, laser-induced fluorescence from polycyclic aromatic hydrocarbons (PAHs) has been reported to interfere with the LII-signal [13, 23], in particular during the onset, <300 ps, of the LII-signal [23]. Fluorescence contributions would affect the evaluated short LII lifetime,  $\tau_{\text{short}}$ . However, fluorescence interference can be effectively avoided using laser wavelength 1,064 nm [13], which has been used in the experiment presented in this paper. In Fig. 5b, the time axis is extended to a range of 165 ns, which corresponds to a spatial range of 25 m. A slower decay, attributed to heat conduction [7, 9, 10, 23, 24], with long lifetime,  $\tau_{\text{long}}$ , dominates the signal after 25 ns, i.e., from 210 ns in Fig. 5b.

The spatial information obtained from LII-lidar measurements is extracted from the time-resolved signal, and depending on the required range resolution, the short or the long lifetime will be of importance for data evaluation. Whereas the short lifetime,  $\tau_{\text{short}}$ , is of importance for soot sources located within a spatial range typically less than 1 m, a combination of short- and long-lifetime contributions needs to be considered for measurements over spatial ranges typically greater than 3 m. The decay constants,  $\alpha$ , for each fluence were calculated as the slopes of the fitted lines, corresponding to the fast and slow decay centered around 190 and 275 ns, respectively. The corresponding lifetimes,  $\tau_{\text{short}}$  and  $\tau_{\text{long}}$ , calculated as  $1/\alpha$ , are presented in Fig. 5c. The ratio  $\tau_{\text{short}}/\tau_{\text{long}}$ , shown as triangles, is fairly constant,  $\sim 3.5$ . Both  $\tau_{\text{short}}$  and  $\tau_{\text{long}}$  decrease with fluence, due to increased sublimation and correspondingly reduced particle size. Employing lower laser fluence, the signal-to-noise ratio decreases which is observed both in the evaluated lifetimes and in the lifetime ratio.



**Fig. 5** a, b Natural logarithm of recorded LII-lidar curves. a Linear fits corresponding to a fast decay time are shown. b The timescale is extended, and linear fits corresponding to a slower decay time are shown centered around 275 ns. The evaluated short and long lifetimes and the ratio  $\tau_{\text{short}}/\tau_{\text{long}}$  for a set of fluences are shown in (c)

For each fluence, the following parameters were calculated from acquired lidar curves: the maximum signal value,  $S_{\max}$ , the maximum time derivative of the signal,  $S'_{\max}$ , and the signal integrated over 800 ns,  $S_{\text{int}}$ . These parameters are plotted versus fluence in Fig. 6, where the curves are normalized in the low fluence range to visualize their qualitative agreement. It is observed that  $S_{\max}$  and  $S'_{\max}$  agree very well, the latter in this case corresponding to the derivative  $G'(t)$  introduced in Sect. 3, since the maximum derivative is obtained for the signal increase part  $G(t)$ . The similarity in trend between  $S'_{\max}$  and  $S_{\max}$  and the coupling between the maximum LII-signal and soot volume fraction,  $f_v$ , will be utilized in Sect. 4.3 for evaluation of range-resolved soot volume fraction profiles from LII-lidar data by means of differentiation. A relative decrease is observed for  $S_{\text{int}}$  toward higher fluences, which agrees well with the shorter lifetimes obtained for higher fluences (cf. Fig. 5c). However, after normalization with the long lifetime,  $S_{\text{int}}/\tau_{\text{long}}$  (dotted curve) agrees very well in shape with  $S_{\max}$  and  $S'_{\max}$ . All curves show an increasing trend up to the maximum laser fluence around  $0.22 \text{ J/cm}^2$ , resembling the prompt LII-signal obtained with nanosecond laser pulses in a similar flame [25]. At even higher fluences, the LII-signal can be expected to level off due to increased sublimation [7].

#### 4.2 Equivalence ratio dependence

To investigate the influence of soot volume fraction,  $f_v$ , and particle size on the LII-lidar signal, measurements were made for flame equivalence ratios,  $\Phi$ , ranging from 1.8 to 3. Data sets were acquired for two laser fluences, 0.1 and  $0.2 \text{ J/cm}^2$ , corresponding to the lower and higher end of the probed fluence range (cf. Fig. 6). The temporal features of

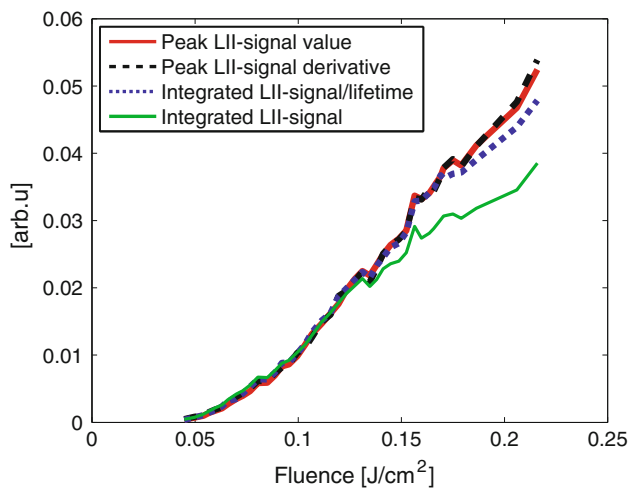


**Fig. 6** Peak LII-signal value,  $S_{\max}$ , peak LII-signal derivative,  $S'_{\max}$ , integrated LII-signal,  $S_{\text{int}}$ , and integrated signal normalized with the long lifetime,  $S_{\text{int}}/\tau_{\text{long}}$ , are plotted versus laser fluence

the LII-lidar curves were the same as shown in Fig. 5b and the parameters,  $S_{\max}$ ,  $S'_{\max}$ ,  $S_{\text{int}}$ , and  $S_{\text{int}}/\tau_{\text{long}}$ , evaluated for the fluence series (Fig. 6), were also calculated for the equivalence ratio series. The results obtained for laser fluence  $0.1 \text{ J/cm}^2$  are presented in Fig. 7a. An excellent agreement in shape is observed between  $S_{\max}$  and  $S'_{\max}$ , whereas  $S_{\text{int}}$  shows a stronger increase with higher  $\Phi$ , which is expected as the lifetimes, particularly  $\tau_{\text{long}}$ , increase with  $\Phi$ . In Fig. 7b, the peak LII-signal is plotted versus  $\Phi$  for laser fluences 0.1 and  $0.2 \text{ J/cm}^2$ . The signal corresponding to the lower laser fluence is roughly one order of magnitude weaker; however, the curve has been normalized versus the maximum value of the higher laser fluence curve. Similar to the data presented in Fig. 6, the integrated signal  $S_{\text{int}}$  has been normalized with the long lifetime,  $\tau_{\text{long}}$  and the  $\Phi$ -dependence of  $S_{\text{int}}/\tau_{\text{long}}$ , shown in

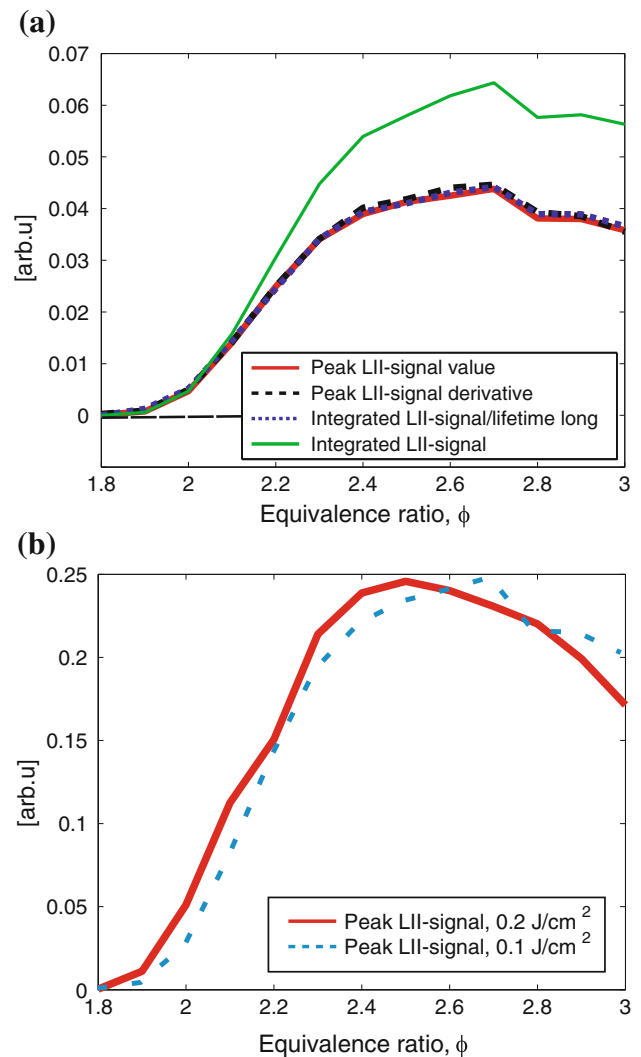


**Fig. 7** **a**  $S_{\max}$ ,  $S'_{\max}$ ,  $S_{\text{int}}$ , and  $S_{\text{int}}/\tau_{\text{long}}$  versus flame equivalence ratio for laser fluence  $0.1 \text{ J/cm}^2$  and **b** normalized  $S_{\max}$  profiles for laser fluences 0.1 and  $0.2 \text{ J/cm}^2$

Fig. 7a, is in very good agreement with that of  $S_{\max}$  and  $S'_{\max}$ .

These kind of flames are reported to show the first indications of soot formation at equivalence ratio  $\Phi = 1.8$  [24] and small LII–lidar signals are observed for  $\Phi = 1.8$  and  $\Phi = 1.9$ . From  $\Phi = 2.0$ ,  $S_{\max}$  increases rather rapidly with  $\Phi$  up to  $\Phi = 2.4$ , followed by a slower increase toward a maximum value and a decrease for the highest equivalence ratios. According to conventional LII experiments in similar flames, both  $f_v$  and the primary particle size increase with  $\Phi$ , in the range  $\Phi = 1.8$  to 2.5 [24]. Hadeef et al. [24] present profiles of soot volume fraction versus height above burner and integration of these data over the height interval probed in the LII–lidar experiments shows an increase in average  $f_v$  by a factor  $\sim 4.6$  between  $\Phi = 2.1$  and  $\Phi = 2.4$ . The LII–lidar data show a weaker increase with a corresponding factor of 2–3; see Fig. 7. One possible factor explaining this could be stronger signal absorption for the back-scattering signal collection geometry of the LII–lidar setup and signal absorption is indicated in the LII–lidar data for the highest equivalence ratios. In addition, other differences between the experiments may have an impact and detailed understanding require more detailed characterization of picosecond LII with backward signal detection. For a flame of equivalence ratio  $\Phi = 2.1$ , Hadeef et al. [24] report an average soot volume fraction of around 0.1 ppm. Comparing this value with the LII–lidar results, obtained over an integration length of 6 cm with an 11 mm diameter laser profile, it can be estimated that the setup permits detection of soot volume fraction levels of  $0.1 \text{ ppm}/6 \text{ cm}/0.95 \text{ cm}^2 = 0.02 \text{ ppm}/\text{cm}/\text{cm}^2$  at a distance of 2 m.

Following the discussion in Sect. 3, evaluation of range-resolved soot volume fraction profiles from LII–lidar data requires information on the decays and lifetimes of the signal, which will be further discussed in Sect. 4.3. The LII–lifetimes,  $\tau_{\text{short}}$  and  $\tau_{\text{long}}$ , are plotted versus equivalence ratio for the low and high laser fluence in Fig. 8a, b, respectively. The results in both figures indicate that the lifetimes, particularly the long lifetimes, increase with  $\Phi$ , in agreement with results from time-resolved LII obtained at specific height in this type of flame and burner [24]. For the lower fluence,  $0.1 \text{ J}/\text{cm}^2$ ,  $\tau_{\text{short}}$  varies between 20 and 40 ns for equivalence ratios in the range  $\Phi = 2$ –3, whereas  $\tau_{\text{long}}$  ranges from 60 to 100 ns. Both lifetimes are reduced at the higher fluence,  $0.2 \text{ J}/\text{cm}^2$ , the values of  $\tau_{\text{short}}$  are rather constant around 20 ns, and the values of  $\tau_{\text{long}}$  are between 55 and 80 ns. Higher laser fluence is expected to increase sublimation, and in turn decrease the particle size, and correspondingly decrease the lifetimes as observed for the data in Fig. 8. As discussed in Sect. 4.1, the impact of the lifetime on LII–lidar data evaluation depends on the distribution of soot sources along the laser beam path and

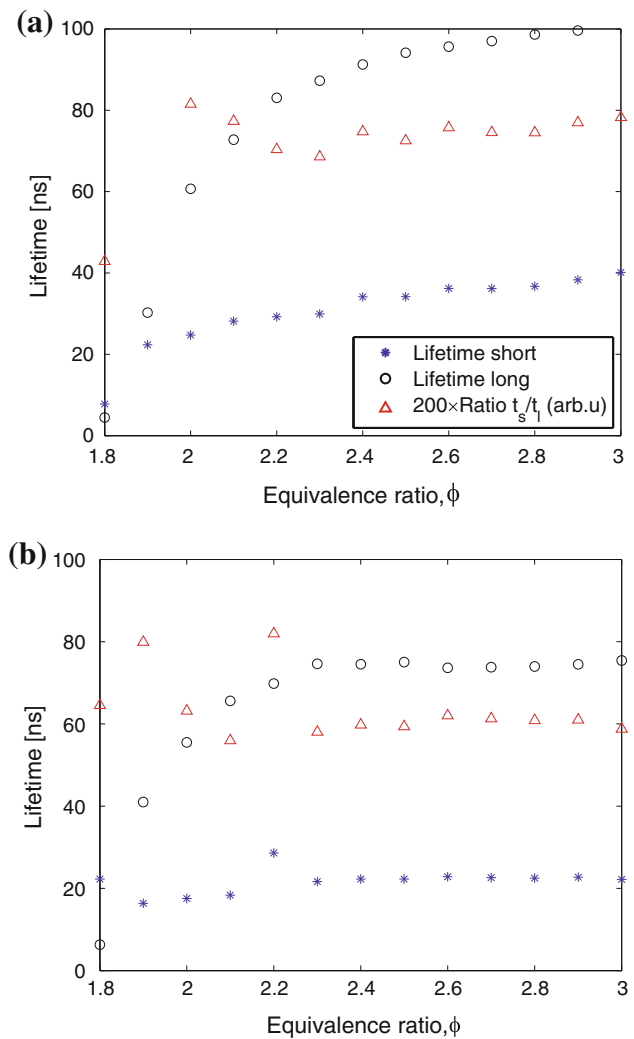


**Fig. 8 a, b** Evaluated short and long LII-signal lifetimes and their ratio  $\tau_{\text{short}}/\tau_{\text{long}}$  for a set of equivalence ratios at laser fluences 0.1 and 0.2 J/cm<sup>2</sup>, respectively

the required range resolution. In the following, this will be exemplified for soot sources located within a range of less than 1 m, corresponding to a time difference of less than 7 ns in the detection. In this case,  $\tau_{\text{short}}$  is the lifetime component dominating the decay, which is clearly illustrated in Figs 5a, b.

#### 4.3 Range-resolved LII–lidar soot volume fraction distributions

The characterization of the LII–lidar signal properties versus laser fluence (Fig. 6) and equivalence ratio (Figs. 7, 8) showed that the maximum derivative  $S'_{\max}$ , corresponding to  $G'(t)$ , is a good representation of the maximum signal  $S_{\max}$  in all investigated cases. Since  $S_{\max}$  is an established measure of soot volume fraction,  $S'_{\max}$  should also be a valid indicator of soot volume fraction.



Two porous-plug-burner flames, with equivalence ratio  $\Phi = 2.1$ , as characterized in Figs. 5c and 6, were placed at different positions along the  $x$ -axis while recording LII-lidar curves, employing laser fluences of 0.07 and 0.19 J/cm<sup>2</sup>, respectively. Such a LII-lidar curve,  $S(t)$ , using laser fluence 0.07 J/cm<sup>2</sup>, is shown, represented by a dashed red line, in Fig. 9a. The burners were positioned 1.75 and 2.15 m from the collection mirror, respectively, which is manifested by two corresponding rising edges in Fig. 9a.

As discussed in Sect. 3 and shown in Sect. 4.1, a signal decay is expected after the laser pulse has passed all soot sources, which can be seen between 2.5 and 4 m in Fig. 9a. Between 2.5 and 3 m, a faster decay is observed corresponding to  $\tau_{\text{short}}$  and between 3 and 4 m a slower decay corresponding to  $\tau_{\text{long}}$  is observed. In the range 1.5–2.5 m, the signal decay, dominated by  $\tau_{\text{short}}$ , is mixed with signal increase contributions from soot sources at different spatial positions. The decay time of interest,  $\tau_{\text{short}}$  can be obtained in three ways: (1) Measuring  $\tau_{\text{short}}$  between 2.5 and 3 m, which will be an overestimation since it is a mix of the long decay from the left peak and the short decay from the right peak. (2) Measuring  $\tau_{\text{long}}$  from 3 m onwards and multiplying with 3 according to the ratios illustrated in Figs. 5c and 8. (3) Using previously known soot characteristics from calibration measurements, such as the data shown in Figs. 5c and 8. In this evaluation,  $\tau_{\text{short}}$  was estimated from Fig. 5c to 32 ns, corresponding to  $\alpha_1 = 31 \times 10^6/\text{s}$ , at fluence 0.07 J/cm<sup>2</sup>, and to 18 ns corresponding to  $\alpha_1 = 55 \times 10^6/\text{s}$  at fluence 0.19 J/cm<sup>2</sup>.

The function  $S_{\alpha=0}(t)$ , indicated with the solid black line in Fig. 9a, is iterated stepwise using the derivative  $G'(t)$  from Eq. (5). At distances  $>3$  m, the compensated time derivative  $G'(t)$  is too high since  $\tau_{\text{long}}$ , corresponding to a lower value on  $\alpha$ , is the dominating decay time. The

overestimation of  $G'(t)$  is manifested in the increase in  $S_{\alpha=0}(t)$  at distances  $>3$  m. The signal,  $S_{\alpha=0}(t)$ , should have been constant if  $\alpha = 0$ . Nevertheless, it is observed that the evaluated  $G'(t)$  works very well for improving the estimation of  $S_{\alpha=0}(t)$  at positions  $<3$  m.

In Fig. 9b,  $S'(t)$  and  $G'(t)$  are plotted and the difference between  $G'(t)$  and  $S'(t)$  is small, since the decay is relatively long compared with the risetime of  $S(t)$ . The small error,  $-\alpha_1 K_{1\tau}$ ,  $-\alpha_2 K_{2\tau}$ , compensated for using only the dominating exponential term corresponding to the decay constant  $\alpha_1$  in Eq. (5), is proportional to the product of the signal level and the decay constant, which makes the error of greater significance when the laser pulse has passed a measurement region with high soot volume fraction. It is observed in Fig. 9b that the maximum error, at the peak of the signal at position 2.25 m, shown in Fig. 9a, is  $<3\%$  of the maximum detected soot volume fraction.

The result of the measurement series employing a laser fluence of 0.07 J/cm<sup>2</sup> is shown in Fig. 10a with the center-to-center distance between the burners indicated in the legend. The left peak of the black solid curve shows the typical appearance of the resulting soot volume fraction above one fully resolved burner. The falltime of the PMT is manifested by a tail on the right side of the peak. As the distance between the burners decreases, the two peaks corresponding to the burners are less resolved.

The highest achievable range resolution (along the laser beam propagation axis) of this particular measurement setup, mainly limited by the detector, has been experimentally estimated to 16 cm. Laser light scattered from two-millimeter-size hard targets was detected, resulting in a signal with two separate peaks. The resolution was defined as the distance, where the signal level between the partially overlapping peaks, was half that of the individual

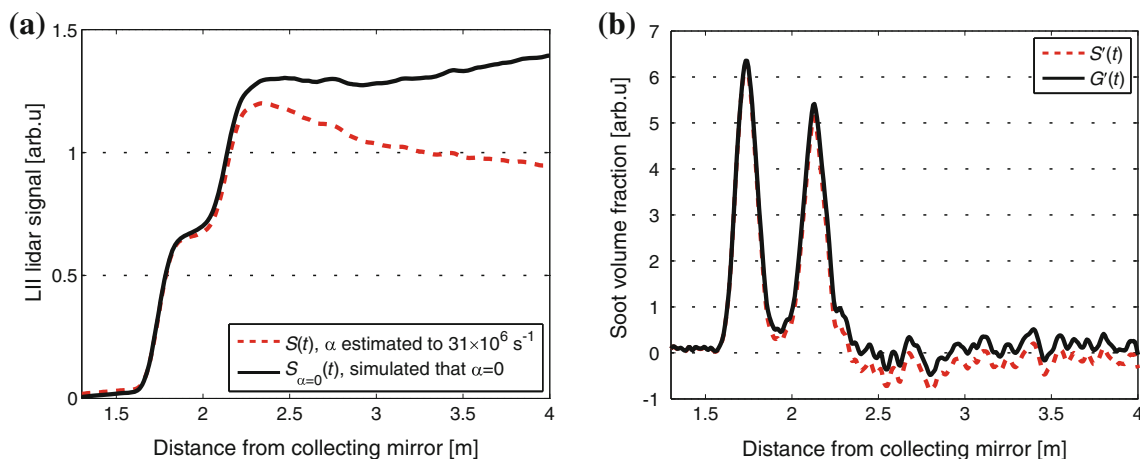


**Fig. 9 a** Acquired LII-lidar signal (dashed red profile) and the corresponding signal obtained through iterative calculations with  $\alpha = 0$  (black solid profile), for burners placed at distances 1.75 and

2.15 m. Details on the analysis are given in “Results and discussion”. **b** Time derivatives, corresponding to soot volume fraction profiles, of the curves in **a**

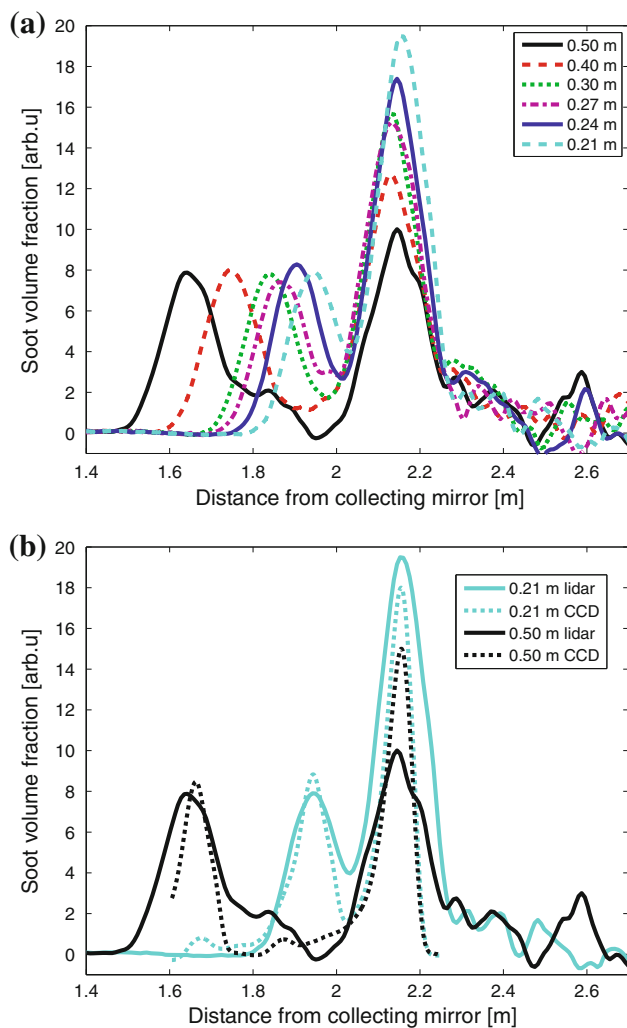


**Fig. 10** **a** Resulting LII-lidar soot volume fraction distributions from two burners, supplied with ethylene–air mixture of  $\Phi = 2.1$ , and having center-to-center distance as indicated in the legend. **b** Soot volume fraction profiles measured with LII-lidar (*solid*) and right-angle ICCD detection (*dashed*) for burner distances 0.21 and 0.50 m. The similarity between corresponding profiles confirms the spatial accuracy of LII-lidar, based on single-ended detection. The laser beam propagates away from the collection mirror, i.e., toward the right in *graphs*

peaks [18]. Taking the spatial extension of the burners, 6 cm diameter, into account makes it probable to expect that the curve corresponding to a distance of 21 cm between the burners is a profile representing the resolution limit of this LII-lidar setup.

The evaluated soot volume fraction curves were normalized using an estimate of the range dependent LII-lidar signal collection efficiency,  $O(R)$ , where  $R$  designates distance from the collecting mirror to the signal source.  $O(R)$  was determined by observing the LII-signal intensity from a soot source placed at different positions along the  $x$ -

axis.  $O(R)$  depends on the focus distance of the primary telescope mirror, M2, the overlap of the laser beam path and the optical axis of the collecting mirror, and the factor  $1/R^2$ , due to isotropic signal sources.

To further validate the LII-lidar results, simultaneous right-angle measurements, using an ICCD camera, were made. Figure 10b shows LII-lidar curves (solid lines) together with corresponding profiles acquired with right-angle ICCD detection (dashed lines) for burner distances 21 and 50 cm. The ICCD data originally had a pixel resolution of 0.1 mm/pixel and have been convoluted with a PMT response curve obtained from measurements of hard-target laser scattering [26]. The peaks evaluated from CCD data are narrower than those of the lidar profiles; possibly, the actual width of the PMT response curve has been underestimated in the profile used for evaluation. However, the positions of the peaks in the lidar and CCD profiles are in good agreement for both distances.

The CCD profiles show that the burner positioned at distance 2.15 m gives a factor  $\sim 2$  stronger LII-signal (caused by imperfections in the burner), which corresponds well with the lidar data acquired at 24 cm distance shown with blue solid line in Fig. 10a. For the 21 cm curve (cyan color), the height of the right burner peak is probably increased due to overlap with the tail of the left burner peak. In the curves corresponding to 27, 30, 40, and 50 cm distance between the burners, respectively, the maximum value of the right peak decreases with distance. The origin of this effect is that the left burner and flame stabilizer obscure an increasing part of the LII-signal in the solid angle of the primary telescope mirror, M2, see photo in Fig. 2. Altogether, the comparison with right-angle detection confirms that spatially accurate LII-data can be acquired with backward detection along the optical line of sight using the LII-lidar concept.

Measurements carried out at higher laser fluence,  $0.19 \text{ J/cm}^2$ , exhibit similar results, but with lower range resolution. In scattering-based lidar, where the signal is proportional to laser intensity and mimics the shape of the laser pulse, the range resolution is determined by the pulse duration. In contrast, the LII-signal shows a more complex dependence on the laser profile in time and space. For example, “hole-burning” effects due to sublimation may be observed for high fluences obtained at the center of the pulse [11], resulting in an instantaneous LII-signal with a shape different than the laser pulse. Furthermore, Bladh et al. [11] have observed that the FWHM of a backward LII-signal increase substantially with laser fluence. Such additional complexities suggest that LII-lidar measurements should be carried out maintaining the laser fluence as low as possible.

## 5 Conclusions

A concept for single-ended remote detection of soot, combining laser-induced incandescence (LII) with ps-lidar has been presented. The LII–lidar signal dependence on laser fluence and ethylene–air flame equivalence ratio shows good qualitative agreement with data reported in literature. Analysis of the LII–lidar signal showed that the derivative was proportional to the maximum value, which is established as an adequate measure of soot volume fraction. Utilizing this fact, differentiation of LII–lidar curves gave profiles representing soot volume fraction with a range resolution of  $\sim 16$  cm, determined by the detector characteristics. The range resolution of the lidar measurements was confirmed by a very good agreement with simultaneously measured data using conventional right-angle detection. Comparing with calibrated LII measurements in similar flames, it was estimated that soot volume fraction levels around  $0.02$  ppm/cm/cm<sup>2</sup> can be detected at a distance of 2 m. In conclusion, the LII–lidar technique opens up new possibilities for spatially resolved in situ measurements of soot and other absorbing particles under conditions with limited optical access in power plants, industrial furnaces, and heavy-duty-ship diesel engines.

**Acknowledgments** The authors would like to thank the Centre of Combustion Science and Technology (CECOST) and the European Research Council Advanced Grant DALDECS for financial support. Moreover, Henrik Bladh, Per-Erik Bengtsson, and Jonathan Jonsson should be acknowledged for their input when planning the experiments and their valuable and helpful information regarding LII reference work.

## References

1. H. Bockhorn, *Soot Formation in Combustion—Mechanisms and Models* (Springer, Berlin, Heidelberg, 1994), p. 606
2. A. D'Anna, *Proc. Combust. Inst.* **32**, 593 (2009)
3. G. Shrestha, S.J. Traina, C.W. Swanston, *Sustainability* **2**, 294 (2010)
4. B. Nowack, T.D. Bucheli, *Environ. Pollut.* **150**(1), 5 (2007)
5. P.H. McMurry, *Atmos. Environ.* **34**(12–14), 1959 (2000)
6. H. Moosmuller, R.K. Chakrabarty, W.P. Arnott, *J. Quant. Spectrosc. Radiat.* **110**(11), 844 (2009)
7. C. Schulz, B.F. Kock, M. Hofmann, H. Michelsen, S. Will, B. Bougie, R. Suntz, G. Smallwood, *Appl. Phys. B* **83**, 333 (2006)
8. R.J. Santoro, C.R. Shaddix, in *Applied Combustion Diagnostics*, ed. by K. Kohse-Köinghaus, J.B. Jeffries (Taylor & Francis, London, 2002), pp. 252–286
9. L.A. Melton, *Appl. Opt.* **23**, 2201 (1984)
10. H. Bladh, J. Johnsson, P.-E. Bengtsson, *Appl. Phys. B* **90**, 109 (2008)
11. H. Bladh, P.-E. Bengtsson, J. Delhay, Y. Bouvier, E. Therssen, P. Desgroux, *Appl. Phys. B* **83**, 423 (2006)
12. J.D. Black, Laser-induced Incandescence Measurements of Particles in Aero-Engine Exhausts, EOS/SPIE Meeting, Munich, June 14–18, Paper 3821-38 (1999)
13. K. Schäfer, J. Heland, D.H. Lister, C.W. Wilson, R.J. Howes, R.S. Falk, E. Lindermeier, M. Birk, G. Wagner, P. Haschberger, M. Bernard, O. Legras, P. Wiesen, R. Kurtenbach, K.J. Brockmann, V. Kriesche, M. Hilton, G. Bishop, R. Clarke, J. Workman, M. Caola, R. Geatches, R. Burrows, J.D. Black, P. Hervé, *J. Vally, Appl. Opt.* **39**, 441 (2000)
14. J. Delhay, P. Desgroux, E. Therssen, H. Bladh, P.-E. Bengtsson, H. Hönen, J.D. Black, I. Vallet, *Appl. Phys. B* **95**, 825 (2009)
15. T.P. Jenkins, J.L. Bartholomew, P.A. DeBarber, P. Yang, J.M. Seitzman, R.P. Howard, AIAA, Paper 2002-3736 (2002)
16. C. Weitkamp (ed.), *Lidar Range-Resolved Optical Remote Sensing of the Atmosphere* (Springer, Berlin, 2005)
17. T. Fujii, T. Fukuchi (eds.), *Laser Remote Sensing* (Taylor & Francis, London, 2005)
18. B. Kaldvee, A. Ehn, J. Bood, M. Aldén, *Appl. Opt.* **48**, B65 (2009)
19. B. Kaldvee, J. Bood, M. Aldén, *Meas. Sci. Technol.* **22**, 125302 (2011)
20. D.J. Bradley, B. Liddy, W.E. Sleat, *Opt. Commun.* **2**, 391 (1971)
21. M.Ya. Schelev, M.C. Richardson, A.J. Alcock, *Appl. Phys. Lett.* **18**, 354 (1971)
22. H.A. Michelsen, *J. Chem. Phys.* **118**, 7012 (2003)
23. H.A. Michelsen, *Appl. Phys. B* **83**, 443 (2006)
24. R. Hadeif, K.P. Geigle, W. Meier, M. Aigner, *Int. J. Therm. Sci.* **49**, 1457 (2010)
25. S. Maffi, S. De Iuliis, F. Cignoli, G. Zizak, *Appl. Phys. B* **104**(2), 357 (2011)
26. B. Kaldvee, C. Brackmann, J. Bood, M. Aldén, *Opt. Express* **20**, 20688 (2012)